

Polarimetric Radar Characteristics of Simulated and Observed Intense Convective Cores for a Midlatitude Continental and Tropical Maritime Environment

TOSHI MATSUI,^{a,b} BRENDA DOLAN,^c TAKAMICHI IGUCHI,^{a,b} STEVEN A. RUTLEDGE,^c
WEI-KUO TAO,^a AND STEPHEN LANG^{a,d}

^a *NASA Goddard Space Flight Center, Greenbelt, Maryland*

^b *Earth System Science Interdisciplinary Center, University of Maryland, College Park, College Park, Maryland*

^c *Department of Atmospheric Science, Colorado State University, Fort Collins, Colorado*

^d *Science Systems and Applications, Inc., Lanham, Maryland*

(Manuscript received 16 August 2019, in final form 22 January 2020)

ABSTRACT

This study contrasts midlatitude continental and tropical maritime deep convective cores using polarimetric radar observables and retrievals from selected deep convection episodes during the MC3E and TWICE field campaigns. The continental convective cores produce stronger radar reflectivities throughout the profiles, while maritime convective cores produce more positive differential reflectivity Z_{dr} and larger specific differential phase K_{dp} above the melting level. Hydrometeor identification retrievals revealed the presence of large fractions of rimed ice particles (snow aggregates) in the continental (maritime) convective cores, consistent with the Z_{dr} and K_{dp} observations. The regional cloud-resolving model simulations with bulk and size-resolved bin microphysics are conducted for the selected cases, and the simulation outputs are converted into polarimetric radar signals and retrievals identical to the observational composites. Both the bulk and the bin microphysics reproduce realistic land and ocean (L-O) contrasts in reflectivity, polarimetric variables of rain drops, and hydrometeor profiles, but there are still large uncertainties in describing Z_{dr} and K_{dp} of ice crystals associated with the ice particle shapes/orientation assumptions. Sensitivity experiments are conducted by swapping background aerosols between the continental and maritime environments, revealing that background aerosols play a role in shaping the distinct L-O contrasts in radar reflectivity associated with raindrop sizes, in addition to the dominant role of background thermodynamics.

1. Introduction

It is well known that continental deep convection is more vigorous than maritime convection (Williams and Stanfill 2002; Williams et al. 2004). Continental convection is characterized by stronger vertical velocities and wider convective cores (Lucas et al. 1994). Due to intense updraft velocities, continental convection tends to loft more supercooled water that enhances ice formation (Williams et al. 2005). Consequently, satellite observations show more frequent lightning flashes and heavily rimed hydrometeor signals over continents than oceans (Williams and Stanfill 2002; Williams et al. 2004; Zipser et al. 2006; Stolz et al. 2015).

Williams and Stanfill (2002) argue that the physical origin of continental convective vigor can be ultimately attributed to a higher Bowen ratio (the ratio of

sensible heat flux and latent heat flux). In a continental environment, this dry, hot air generates a deeper boundary layer, supporting the generation of a wider convective plume (Morton et al. 1956). The larger Bowen ratio also elevates convective cloud base height, suppressing warm precipitation processes but enhancing mixed-phase precipitation processes, denoting the thermodynamic effect (Williams and Stanfill 2002). The contrast in Bowen ratio between land and ocean environments can also induce sea-breeze dynamics to enhance deep convection over islands, denoted as the “thermal patch” effect (Robinson et al. 2011).

In addition to the thermodynamic contrast, continental environments are also characterized with more cloud condensation nuclei (CCN) and ice-forming nuclei (IFN) than oceanic due to more aerosol emission sources and well-mixed deep boundary layers (Winker et al. 2013). This could suppress warm rain processes, while enhancing ice aloft and subsequently cold rain

Corresponding author: Toshi Matsui, toshihisa.matsui-1@nasa.gov

processes in deep convection (e.g., Lin et al. 2006). There are numerous observational and numerical simulation studies that support the aerosol hypothesis (reviewed in Tao et al. 2012; Fan et al. 2016). However, it is always difficult to remove the covariance between the thermodynamic factors and aerosols in the observations (Grabowski 2018) even if observational studies stratified these factors (e.g., Lin et al. 2006; Stolz et al. 2015).

Recently, Matsui et al. (2016, hereafter MA16), summarized the land–ocean (L–O) contrast in shallow-to-deep tropical convection signals from a 14-yr climatology in the multisensor satellite signals from the Tropical Rainfall Measuring Mission (TRMM). The observational results confirmed previous findings, including

- continental conditions tend to produce more frequent deep convection and suppressed warm rain processes,
- continental shallow convection tends to have smaller raindrop sizes than maritime shallow convection due to suppressed coalescence processes,
- continental deep convective signals indicate the presence of larger precipitating ice aloft than maritime deep convection, and
- these distinct L–O convective contrast are evident regardless of season and year over the tropics.

MA16 also evaluated the L–O contrast from global storm-resolving models and found that the thermal-patch effect is important for the higher frequency of deep convection events over land, while the thermodynamic effect is important for enhanced ice aloft in continental deep convection.

Liu et al. (2019) examined individual as well as combined impact of thermodynamic parameters on the geographical distributions of high-flash rate thunderstorm. The results suggest the probability of these events are predicted poorly by an individual parameter, but predicted skillfully by the combination of four parameters: convective available potential energy (CAPE), convective inhibition (CIN), low-level wind shear, and warm cloud depth, including the strong L–O contrast of likelihood in high-flash rate thunderstorm.

Previous satellite observational studies mostly used radar reflectivity, microwave brightness temperature, and lightning flash counts observed from the TRMM satellite (Williams and Stanfill 2002; Williams et al. 2004; Zipser et al. 2006; Stolz et al. 2015; Matsui et al. 2016; Liu et al. 2019). The previous numerical modeling studies of L–O contrast used cloud-resolving simulations with simple bulk microphysics schemes without specification of background aerosols (Robinson et al. 2011; MA16). To understand the L–O contrast in deep convection further, it is essential to quantify physical quantities and processes, which has not been achieved

in previous studies (summarized in MA16) with more explicit quantification of cloud microphysics associated with hydrometeor types, and relative roles of aerosols for convective vigor.

In this paper, polarimetric radar measurements and retrievals are used to characterize the L–O contrast of deep convective cores from carefully selected continental and maritime cases using more sophisticated cloud-resolving simulations with size-resolving bin microphysics. The paper is organized as follows. In section 2, the field campaigns for the cases used to study the L–O contrast, TRMM satellite composites, and numerical cloud-resolving model with bulk and bin microphysics, a polarimetric radar simulator are described. In section 3, observed and simulated L–O composites of polarimetric radar signals and retrievals from the selected cases are described. Section 4 shows the impact of background aerosols on polarimetric radar L–O composites. The summary and discussion are given in section 5.

2. Field campaigns and numerical experiments

a. Midlatitude continental and tropical maritime cases

Unlike satellite observations, high-quality polarimetric radar measurements are available only in particular locations. This study focuses on cases collected during two field campaigns: the Tropical Warm Pool–International Cloud Experiment (TWP-ICE; May et al. 2008) and the Midlatitude Continental Convective Clouds Experiment (MC3E; Jensen et al. 2016). TWP-ICE, hereafter just TWPICE, took place in austral summer 2006 near Darwin, Australia, to capture tropical maritime convection with a number of ground- and aircraft-based observations. The TWPICE field campaign included a polarimetric C-band radar (CPOL) at Gunn point and a Doppler C-band radar 25 km away at Berrimah. Data from these radars can be used to retrieve rainfall rates, bulk hydrometeor identification (HID), and 3D winds using dual-Doppler techniques (Collis et al. 2013; Dolan et al. 2013).

MC3E took place in boreal spring 2011 near the Atmospheric Radiation Measurement (ARM) Southern Great Plains (SGP) site in north-central Oklahoma, United States, to observe midlatitude continental convection and better understand convective life cycles (Jensen et al. 2016). MC3E was a joint effort between the Department of Energy (DOE) ARM program and the NASA Global Precipitation Measurement Ground Validation (GV) program. It included multiple polarimetric radars (S, C, X, and Ka) and wind profilers with a dense array of surface disdrometers and rain gauges. In situ aircraft sampling was provided by the University of

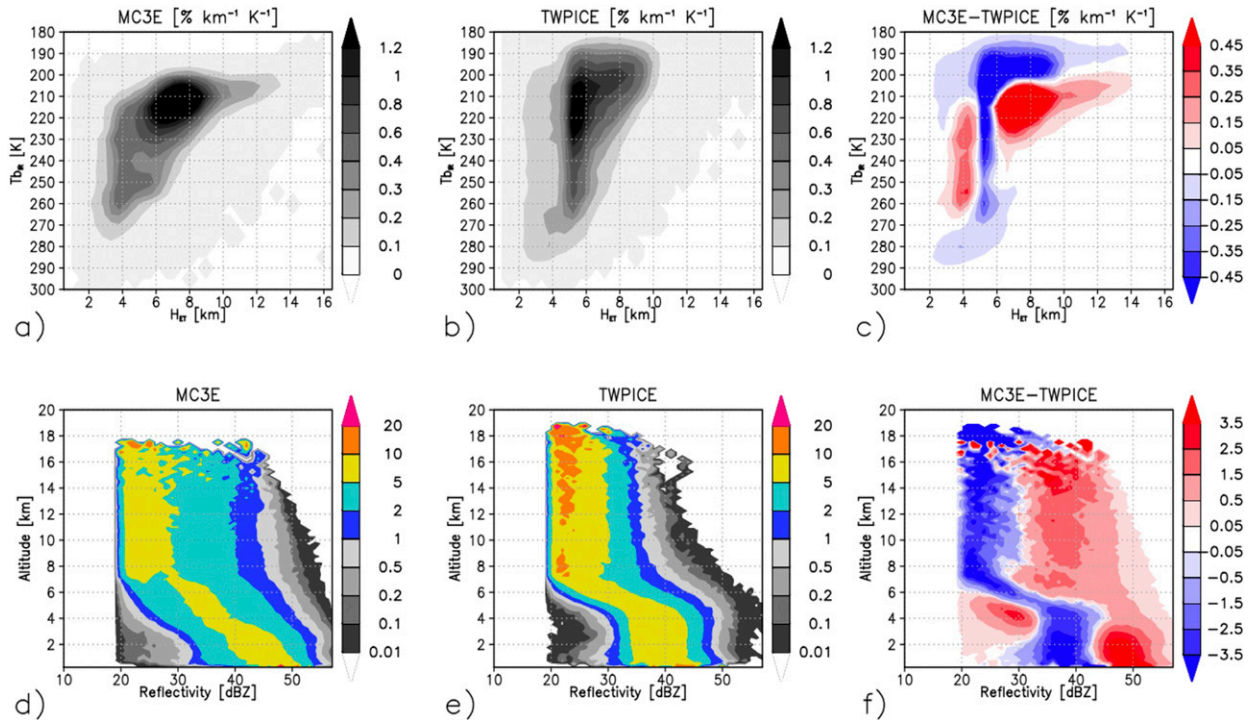


FIG. 1. The 14-yr climatology of TRMM multisensor composites sampled over the MC3E and TWIPICE regions following the method and the database described in MA16. (top) Joint diagrams of 12- μm IR $T_{b_{\text{IR}}}$ and PR 13.8-GHz radar top height (greater than 20 dBZ) for (a) MC3E, (b) TWIPICE, and (c) MC3E-TWIPICE contrast. (bottom) CFADs of PR 13.8-GHz radar reflectivity from deep convective cores for (d) MC3E, (e) TWIPICE, and (f) MC3E-TWIPICE contrast.

North Dakota (UND) citation aircraft. This study primarily relies on the C-band Scanning ARM Precipitation Radar (C-SAPR) radar in order to quantitatively compare polarimetric radar measurements and retrievals with the CPOL radar in TWIPICE. In addition to C-SAPR, two ARM X-band radars (X-SAPRs) are also used for multiple-Doppler retrievals.

Figure 1 shows the 14-yr climatology of TRMM multisensor composites sampled over the MC3E (30°–35°N and 101°–96°W in May only) and TWIPICE (30°–35°N and 101°–96°W in January only) domains, following the method and the database described in MA16. Figures 1a–c show joint diagrams of TRMM Visible Infrared Scanner (VIRS) 12- μm infrared (IR) brightness temperature ($T_{b_{\text{IR}}}$) and TRMM precipitation radar (PR) 13.8-GHz radar top height H_{ET} for MC3E, TWIPICE, and their respective differences. The radar top height H_{ET} is determined as having three successive layers (250-m vertical bins) of significant PR reflectivity (i.e., a 20-dBZ threshold) and is calculated from above ground level using a 5-km mesh digital elevation map. This joint $T_{b_{\text{IR}}}$ - H_{ET} diagram is useful for identifying precipitating cloud types in continental and maritime environments (Masunaga and Kummerow 2006; Matsui et al. 2009; MA16).

Figures 1a and 1b illustrate that the MC3E region tends to have higher H_{ET} than TWIPICE, while TWIPICE tends to have colder $T_{b_{\text{IR}}}$ than MC3E. The MC3E-TWIPICE difference plot highlights that TWIPICE (MC3E) H_{ET} is narrowly concentrated at 5 km (4 km) above ground level in association with the differing freezing level heights in the two regions. Figures 1d and 1e show contoured frequency with altitude diagrams (CFADs; Yuter and Houze 1995) of TRMM PR attenuation-corrected reflectivity profiles sampled with the criteria that H_{ET} is greater than 7 km and no melting band is evident. The MC3E-TWIPICE differences show that MC3E tends to have stronger reflectivities throughout the profiles, particularly above 6 km in height. Below the 6-km level, the TWIPICE PR reflectivities are more narrowly distributed than for MC3E (Fig. 1f).

Two case studies, one from MC3E and one from TWIPICE, were selected for deeper analysis. For TWIPICE, a mesoscale convective system (MCS) occurring during the active monsoon on 23–24 January, dubbed “Landphoon John” (May et al. 2008), is selected to represent tropical maritime convection, while the 23–24 May supercell case from MC3E (Jensen et al. 2016) is chosen to characterize midlatitude continental convection. The Landphoon John

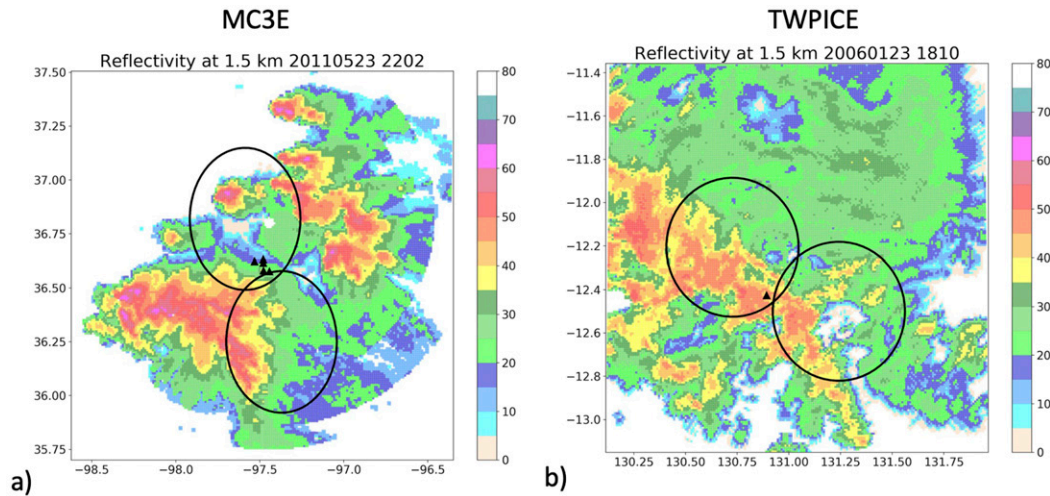


FIG. 2. Observational domains and observed radar reflectivity from the selected MC3E (2202 UTC 23 May 2011) and TWPICE (1810 UTC 23 Jan 2006) cases. Closed triangles represent the location of ground disdrometers.

event has been simulated by many previous modeling studies (Fridlind et al. 2012; Zhu et al. 2012; Varble et al. 2014). The MC3E supercell case was used to introduce a polarimetric radar simulator and to study aerosol interactions using WRF with size-resolved microphysics (Matsui et al. 2019; Iguchi et al. 2019, manuscript submitted to *J. Geophys. Res. Atmos.*). These two locations were selected to study L-O contrast to make use of the polarimetric radars, making the comparison specifically between tropical maritime and midlatitude continental convection similar to Wang et al. (2019), but unlikely the previous satellite observational studies (Williams and Stanfill 2002; Williams et al. 2004; Zipser et al. 2006; Stolz et al. 2015; MA16). However, MC3E–TWPICE contrast is denoted as L-O contrast for simplicity in this manuscript.

Figure 2 shows the observation domains and instantaneous radar reflectivity from the selected MC3E and TWPICE cases (Dolan et al. 2013). Hereafter, convective and stratiform storm elements are separated using the method of Steiner et al. (1995) on the basis of the intensity and sharpness of the peaks in radar reflectivity intensity. Both events have intense convective cores as measured by the high reflectivities (>50 dBZ). However, it should be noted that the MC3E case's convective cores were not well captured by the disdrometers, which impacts the statistical comparison between the MC3E and TWPICE cases later. Because of this limitation, the disdrometer-based analysis periods are extended sampled from 3 November 2005 to 10 February 2006 for TWPICE and from 23 April to 25 May 2011 for MC3E beyond these two events during the MC3E and TWPICE campaigns.

Figure 3 shows time series of domain-mean conditional (sampled at raining pixels only) rainfall rates in

the MC3E and TWPICE cases for convective, stratiform, and total grids, estimated by the aforementioned scanning radars (C-SAPR in MC3E and CPOL in TWPICE). The domain is depicted in Fig. 2. Conditionally averaged instantaneous convective rainfall rates for the MC3E and TWPICE cases peak at approximately 9 and 14 mm h⁻¹ during the time periods, respectively. Hereafter, time-integrated statistical results from the radar observations shown herein focus on the shaded time windows during active periods to characterize the dynamic and

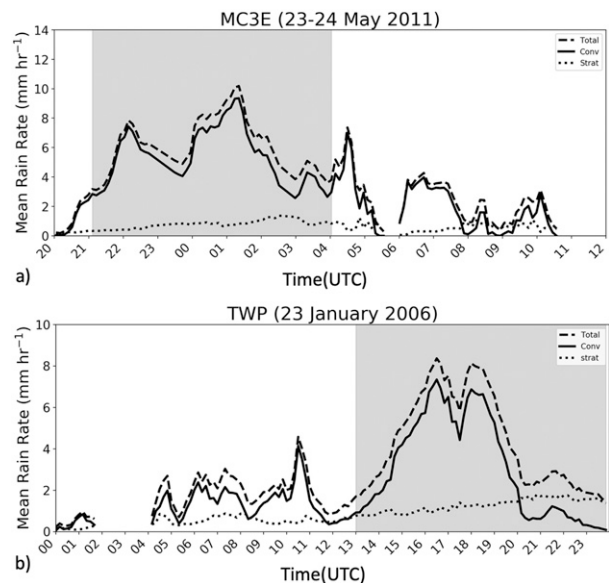


FIG. 3. Time series of conditional (sampled at rain pixels only) convective and stratiform rainfall rates for the selected MC3E and TWPICE cases. Shaded areas represent active convective periods used for characterizing the statistical composites of convective cores.

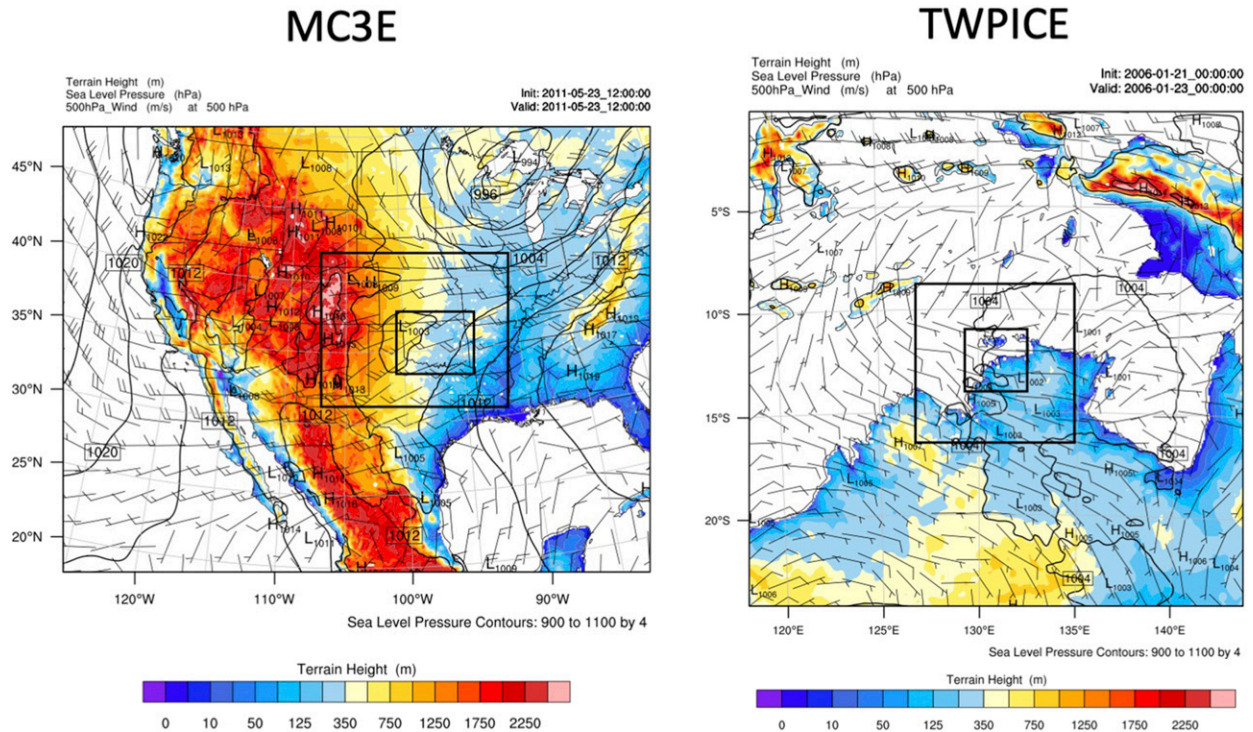


FIG. 4. WRF triple-nested domains with background terrain height (color shaded), surface pressure (contours), and 500-hPa-level wind vectors (arrows) for the (a) MC3E and (b) TWIPICE cases.

microphysical signals of intense convective cores between the continental and the maritime environments.

b. Numerical experiment with cloud-resolving model

This study uses the Advanced Research Weather Research and Forecasting Model (WRF-ARW; Michalakes et al. 2001; Skamarock et al. 2008). Figure 4 shows triple-nested domains set up for the MC3E and TWIPICE cases with 9-, 3-, and 1-km grid spacings. The WRF simulations are initialized and forced by National Centers for Environmental Prediction (NCEP) Global Forecasting System (GFS) and the European Centre for Medium-Range Weather Forecasts (ECMWF) interim reanalysis for the MC3E and TWIPICE cases, respectively, based on the initial diagnosis of simulation evaluations with several different initial and lateral boundary conditions (not shown here). Detailed setups are discussed more in Iguchi et al. (2019, manuscript submitted to *J. Geophys. Res. Atmos.*).

Skew- T plots are derived from the centers of the WRF domains one hour prior to the convective initiation (Fig. 5). Both the MC3E and TWIPICE skew- T plots show wet and warm surface conditions with strong wind shear, both of which are critical for generating organized deep convection (e.g., Houze and Betts 1981). Near-surface temperature and humidity in the MC3E skew- T

plot are similar to those for TWIPICE, but the middle troposphere is drier and colder in MC3E than TWIPICE. As a result, MC3E buoyancy (area between the solid black line and dotted red line) is concentrated between the 700 and 150 hPa levels. In contrast, the TWIPICE buoyancy profile is narrower than the MC3E but deeply distributed from the surface to beyond 100 hPa, which likely generate taller but lesser intense deep convection in the TWIPICE environment in contrast to the MC3E environment. It most likely appeared in the TRMM joint T_{bIR} - H_{ET} diagram, contrasting between these two regions (Fig. 1c). MC3E CAPE is 5904 J kg^{-1} , while TWIPICE CAPE is 3731 J kg^{-1} . This skew- T plot contrast appears to be very similar to those of Wang et al. (2019), which compared midlatitude and tropical continental thermodynamics.

This study utilizes two microphysical packages: the Goddard single-moment 4ICE microphysics, hereafter 4ICE (Lang et al. 2014; Tao et al. 2016) and the Hebrew University Cloud Modeling Spectral Bin Microphysics (HUCM SBM, hereafter SBM) (Khain et al. 2011; Iguchi et al. 2012a,b, 2014). These schemes calculate the nucleation of droplets and ice crystals, condensation and depositional growth, evaporation, sublimation, droplet freezing, riming, melting, shedding, coalescence growth, and/or breakup of the categorized hydrometeor particles with and without explicit size distribution assumptions.

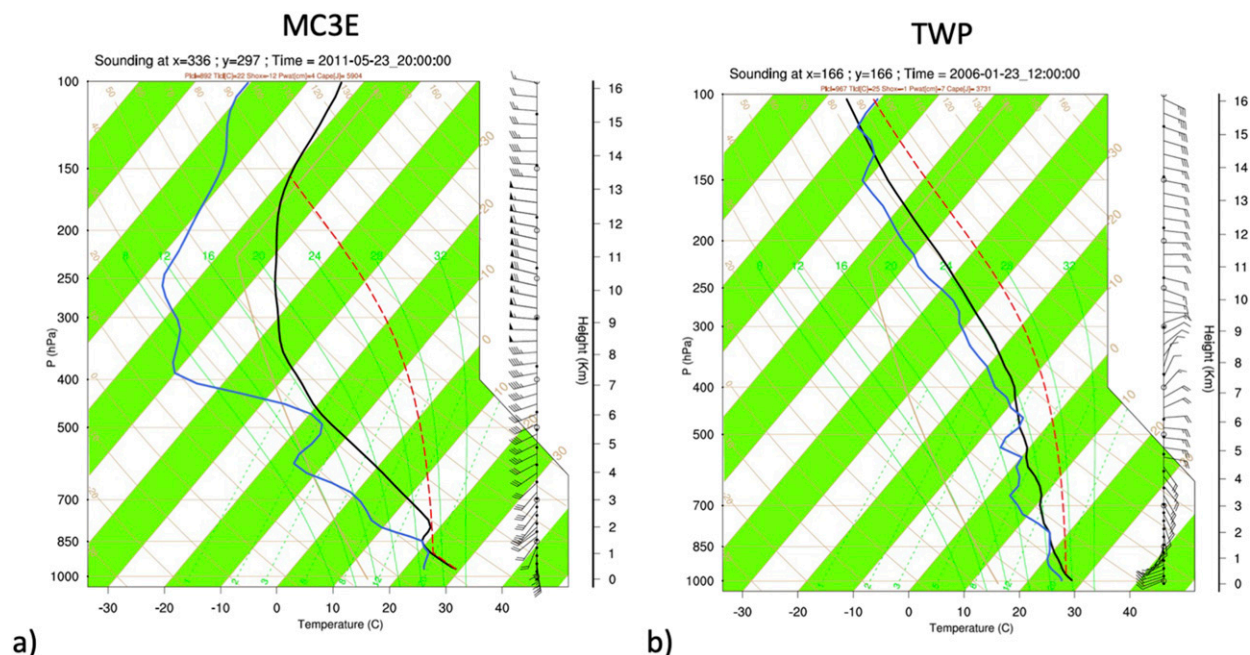


FIG. 5. Skew- T diagrams of prestorm (1 h before storm onset) environmental conditions, sampled at the center of the WRF inner domains for the (a) MC3E and (b) TWICE cases.

The use of 4ICE in this study is motivated by MA16 in which L-O statistics were generated using the NASA Goddard Multi-Modeling Framework (MMF) with 2D 4-km mesh CRMs (Chern et al. 2016; Tao and Chern 2017).

The use of SBM allows for the investigation of the aerosol impact on the MCSs regarding the L-O contrast; previous L-O contrast simulation studies did not include their impact/processes in the simulations (Robinson et al. 2011; MA16). The WRF-SBM simulation is initialized and predicts atmospheric aerosols using the Modern-Era Retrospective Analysis for Research and Applications Aerosol Reanalysis (MERRAero) (Randles et al. 2016). Since the simulations are integrated for short periods, surface emissions are not considered. A detailed methodology is described in Iguchi et al. (2019, manuscript submitted to *J. Geophys. Res. Atmos.*). Table 1 shows the mean CCN concentrations at four pressure levels in the MC3E and TWICE cases at 1% supersaturation. The MC3E(POL) case has up to 50 times larger concentrations of CCN than the TWICE(CLN) case at 850 hPa. This CCN contrast is consistent with typical L-O variations in CCN concentrations (Seinfeld and Pandis 2006).

c. Polarimetric radar simulator

To evaluate the L-O contrasts of the CRM simulations against the polarimetric radar measurements and retrievals, an end-to-end comprehensive synthetic polarimetric-radar simulator, called the Polarimetric

Radar Retrieval and Instrument Simulator (POLARRIS) framework (Matsui et al. 2019) is used (available at <http://radarmet.atmos.colostate.edu/polarris/>). POLARRIS is applied to the CRM outputs to convert CRM geophysical parameters into polarimetric radar observables, which are further converted into retrievals parameters such as HID and precipitation (Dolan and Rutledge 2009; Dolan et al. 2013).

The forward component, denoted as POLARRIS-f, is composed of radar geometry, T-matrix, and Mueller matrix modules (Vivekenandan et al. 1991) for converting WRF-simulated geophysical parameters to polarimetric radar observables and radial velocity (Z_h , Z_{dr} , K_{dp} , ρ_{hv} , V_{rad}). The single scattering matrix of axis-symmetric oblate hydrometeors is computed using the T-matrix. The Mueller matrix uses the single-scattering properties derived from the T-matrix to estimate radar observables using assumed particle

TABLE 1. CCN number concentrations at 1% supersaturation (cm^{-3}) at specific pressure levels for the MC3E and TWICE control and sensitivity experiments. The CCN values are horizontally averaged over the innermost WRF domain.

Pressure level (hPa)	MC3E (POL)	MC3E (CLN)	TWICE (CLN)	TWICE (POL)
925	1398.5	159.8	77.2	1187.5
850	2000.7	47.8	39.3	1963.7
700	638.2	3.8	3.5	610.2
500	146.8	2.5	2.7	148.9

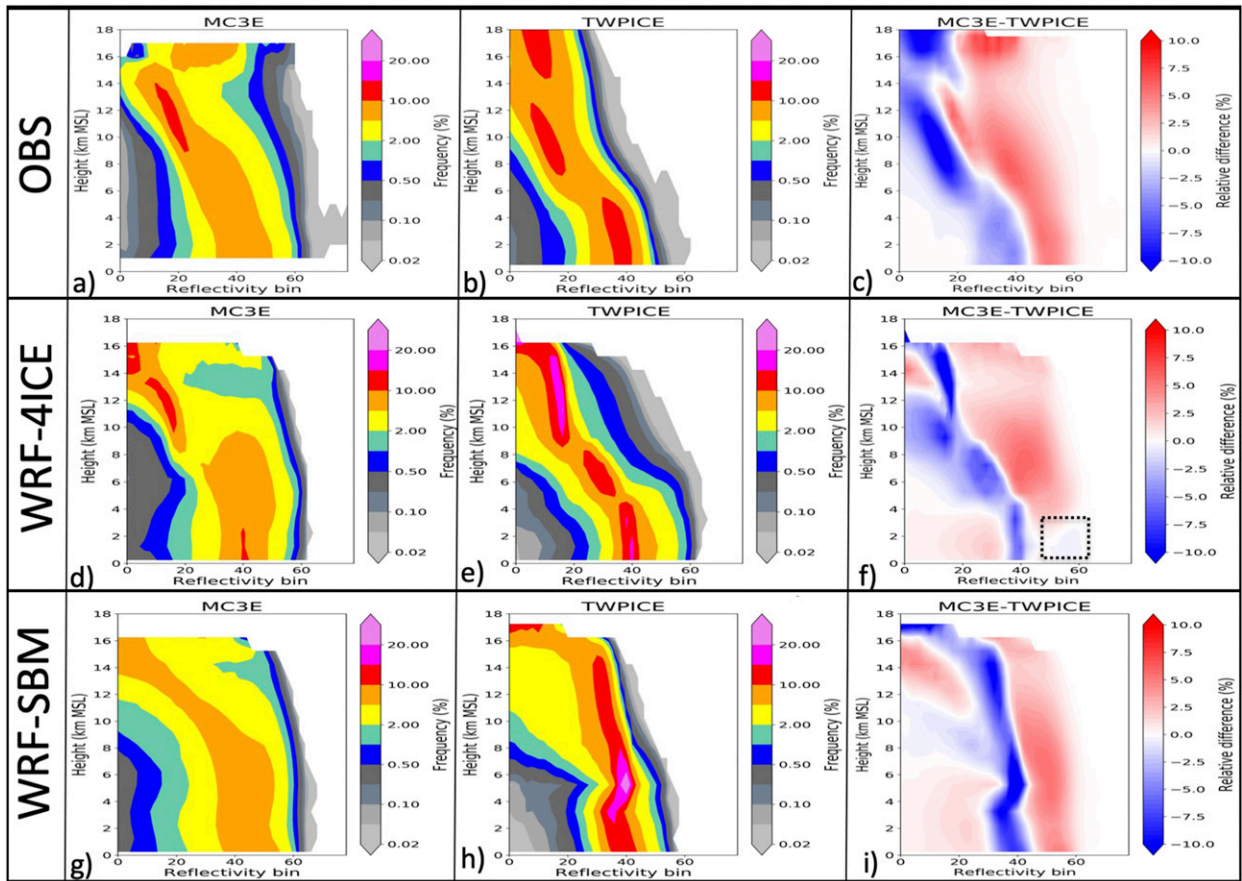


FIG. 6. (top) CFADs of horizontally polarized reflectivity Z_h (dBZ) from (a) MC3E, (b) TWPICE, and (c) MC3E–TWPICE contrast. (middle) POLARRIS-simulated Z_h CFADs from the WRF-4ICE simulation for (d) MC3E, (e) TWPICE, and (f) MC3E–TWPICE contrast. (bottom) POLARRIS-simulated Z_h CFADs from the WRF-SBM simulation for (g) MC3E, (h) TWPICE, and (i) MC3E–TWPICE contrast.

canting angle distributions (Vivekenandan et al. 1991). A microphysics module is then used to integrate the T- and Mueller matrices over the unique particle size assumptions consistent with the CRM’s microphysics in terms of the sizes, densities, and water phase from the bin and bulk microphysics schemes. However, the assumed particle shapes and orientation angle distributions are independently assumed in the forward component, since these properties are not explicitly considered in the bulk and SBM microphysics (Matsui et al. 2019). This often limits the analysis of polarimetric observables above the melting layer. For this study, the assumptions for ice particle shape and orientation angles are from Ryzhkov et al. (2011), but the detailed L-O contrast for Z_{dr} and K_{dp} above the melting layer are not analyzed in this manuscript due to complicated ice hydrometeor shapes and orientations.

The inverse component, denoted as iPOLARRIS, is a set of retrieval algorithms that can be executed on either simulated model data through POLARRIS-f output

(Z_h , Z_{dr} , K_{dp} , ρ_{hv} , V_{rad}) or on polarimetric and dual-Doppler radar observations. In other words, HID can be derived consistently from the observed and simulated polarimetric signals using the same fuzzy logic algorithm, rather than direct CRM outputs of hydrometeor types. The iPOLARRIS framework also generates streamlined statistical analyses of model and observations (Figs. 6–10).

The statistical results in the following sections are taken from WRF-4ICE and WRF-SBM simulations output every 10 min from 2200 UTC 23 May to 0130 UTC 24 May (3.5 h) for MC3E and from 1500 UTC 23 January to 1900 UTC 23 January (4 h) for TWPICE. Note that these timeframes differ from the observation period (Fig. 3) as they are based on the active convective periods in the WRF simulations. Detailed precipitation time series are available in Iguchi et al. (2019, manuscript submitted to *J. Geophys. Res. Atmos.*). Based on the simulated radar signals, iPOLARRIS applies an identical convective–stratiform separation method

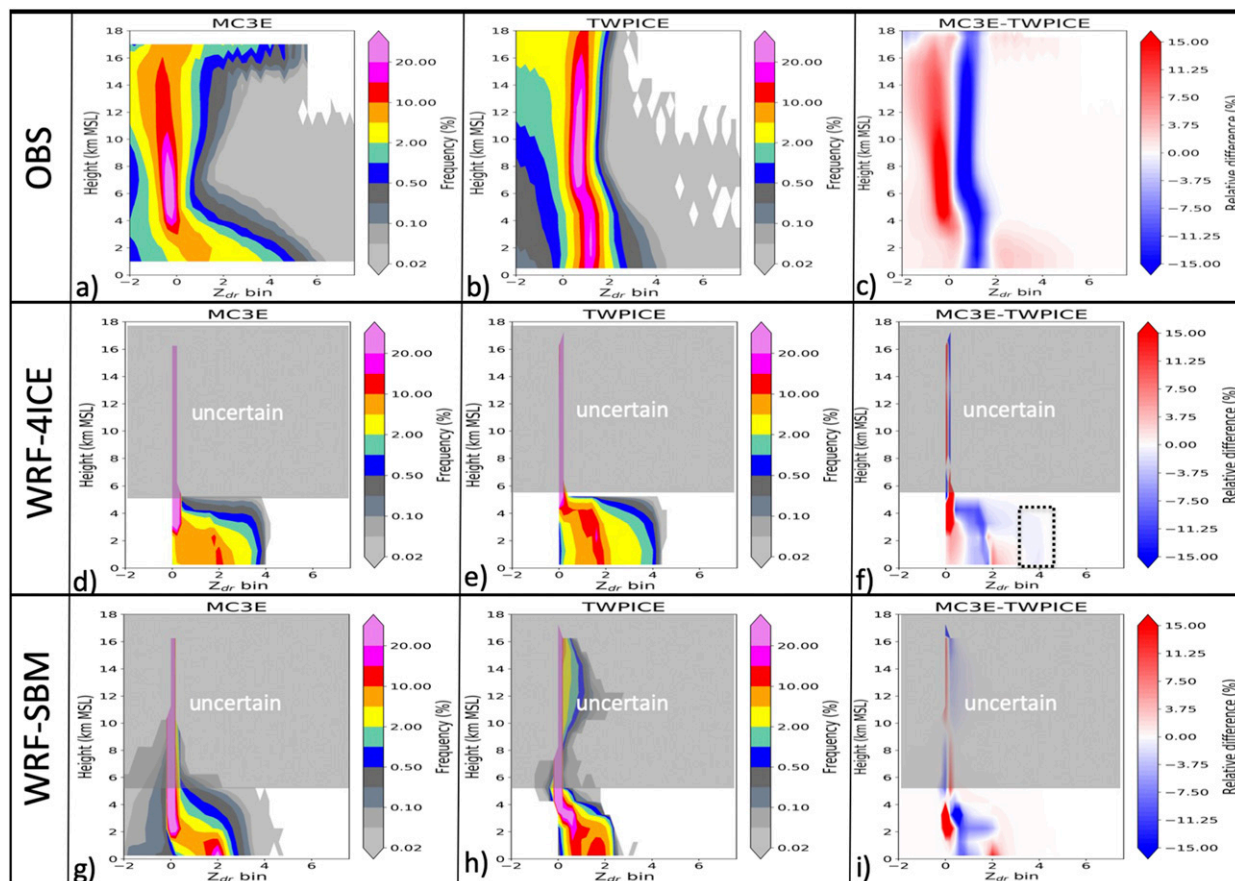


FIG. 7. (top) CFADs of differential reflectivity Z_{dr} from (a) MC3E, (b) TWPICE, and (c) MC3E–TWPICE contrast. (middle) POLARRIS-simulated Z_{dr} CFADs from the WRF-4ICE simulation for (d) MC3E, (e) TWPICE, and (f) MC3E–TWPICE contrast. (bottom) POLARRIS-simulated Z_{dr} CFADs from the WRF-SBM simulation for (g) MC3E, (h) TWPICE, and (i) MC3E–TWPICE contrast.

(Steiner et al. 1995) as was applied to the observations; only the convective cores are examined. In this study, both polarimetric observables and retrievals are interpolated to a 1-km horizontal grid with 500-m constant vertical spacing from the 1-km mesh domains of the WRF simulations for both the MC3E and TWPICE cases. The ensuing statistical analyses and convective–stratiform separation are all conducted on this resolution.

3. MC3E–TWPICE contrast using polarimetric radar measurements and retrievals

a. Observational analysis

In this section, polarimetric radar measurements and retrievals between the MC3E and TWPICE cases are examined. Both sets of radar measurements cover the peak periods of radar-measured deep convection (Fig. 3). Convective and stratiform storm elements are separated using the method of Steiner et al. (1995) using the lowest level of radar reflectivity. This separation

does not account for the echo-top height criteria used for the TRMM satellite (Fig. 1), since this study focuses on periods of organized deep convection both in the observations and the numerical experiments. Hereafter, all the analysis focuses on microphysics characteristics of convective elements only in the MC3E and TWPICE regimes. Alternatively, the statistical analysis does not account for storm sizes or life cycles, which are difficult to measure by the ground-based radar framework.

Figures 6a and 6b show CFADs of horizontally polarized reflectivity Z_h (dBZ) from the MC3E and TWPICE cases. MC3E has more widely distributed CFADs than TWPICE. Figure 6c shows the MC3E–TWPICE difference in CFADs, clearly indicating a shift to stronger Z_h values in MC3E throughout the profile than TWPICE. At upper levels (10–16 km), the MC3E Z_h distributions are stronger than TWPICE by about 20–30 dBZ. Together with near-zero Z_{dr} (Fig. 7a) and K_{dp} (Fig. 8a) values above a height of 4–6 km, this

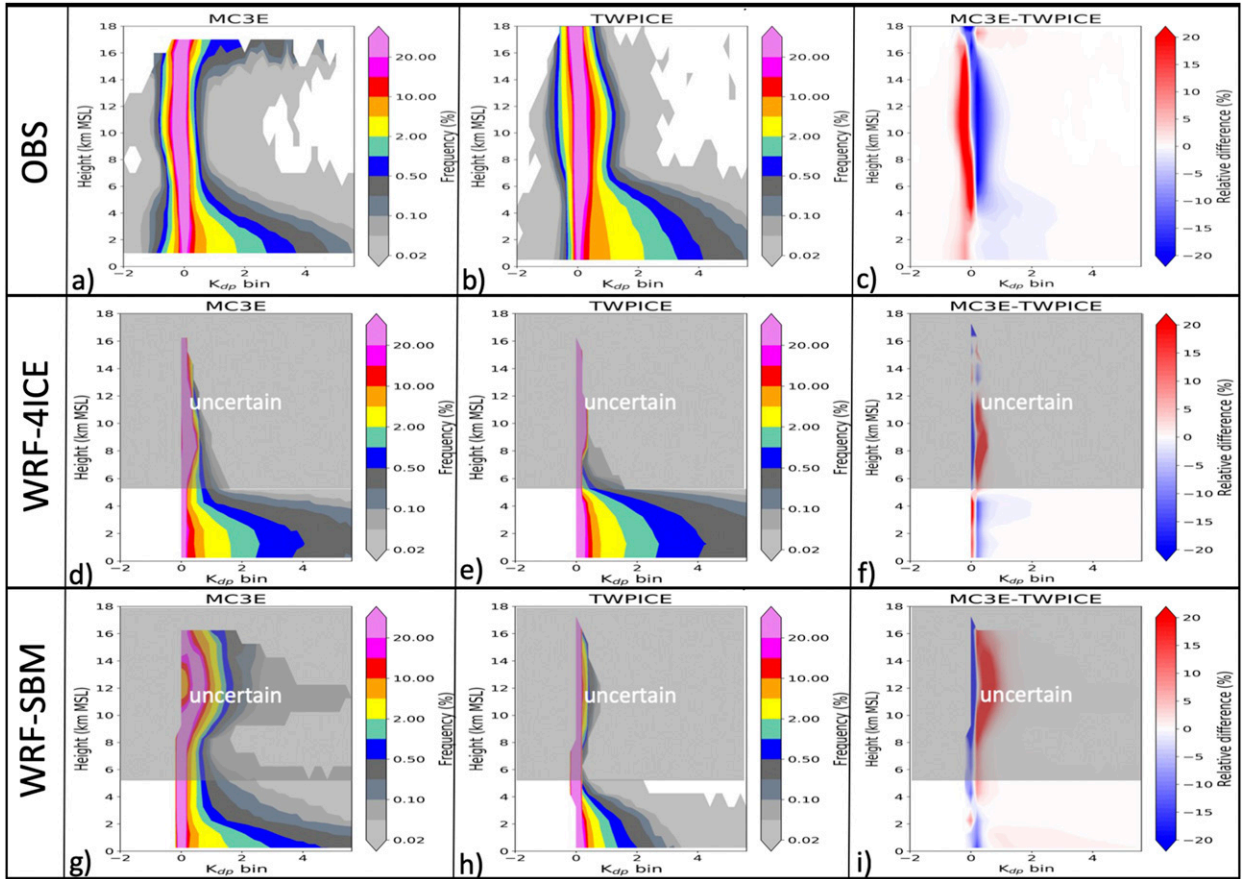


FIG. 8. (top) CFADs of the specific differential phase K_{dp} ($^{\circ}\text{km}^{-1}$) from (a) MC3E, (b) TWPICE, and (c) MC3E–TWPICE contrast. (middle) POLARRIS-simulated Z_{dr} CFADs from the WRF-4ICE simulation for (d) MC3E, (e) TWPICE, and (f) MC3E–TWPICE contrast. (bottom) POLARRIS-simulated Z_{dr} CFADs from the WRF-SBM simulation for (g) MC3E, (h) TWPICE, and (i) MC3E–TWPICE contrast.

strong Z_h values suggests the presence of heavily rimed large ice particles in the MC3E case. On the other hand, TWPICE’s convective core is predominantly characterized with less-rimmed ice (snow aggregates) (discussed in Fig. 9). This L-O contrast in the Z_h CFAD pattern somewhat mimics the climatology derived from the TRMM satellite (Fig. 1f) and also the tropical statistics in MA16, although the convection–stratiform separation method, radar band, sampling area and temporal scale are different from the selected cases. Both show MC3E convective Z_h values being stronger in general. This result demonstrates that the MC3E and TWPICE cases reasonably represent typical continental and maritime deep convective cores.

Figures 7a and 7b show CFADs of differential reflectivity Z_{dr} (dB) for the MC3E and TWPICE cases. Differential reflectivity Z_{dr} is a measure of the size-weighted mean oblateness of particles and is also sensitive to particle phase (liquid versus ice). The MC3E

case shows narrow Z_{dr} distributions centered around zero from 5- to 10-km height. The Z_{dr} is more broadly distributed toward positive values below 5 km in height due to the presence of oblate rain drops or melting hail. The TWPICE case shows narrower and more uniform vertical distributions in Z_{dr} than the MC3E case. Negative Z_{dr} values appear at 10 km and higher heights due to the presence of either lightning-induced vertically oriented columnar ice crystals or radar attenuation issues in both the MC3E and TWPICE cases. Negative Z_{dr} values that appear below 10 km in the MC3E case are due to a radar attenuation issue or resonance scattering associated with melting hail. The MC3E–TWPICE difference plot shows modal Z_{dr} values in the TWPICE case are larger than the MC3E above 4 km. Below 4 km, the MC3E case has broader Z_{dr} distributions, meaning raindrop sizes in the continental convection are stretched to both smaller and larger values (Fig. 7c) possibly due to size sorting or melting hail (see discussion in section 5).

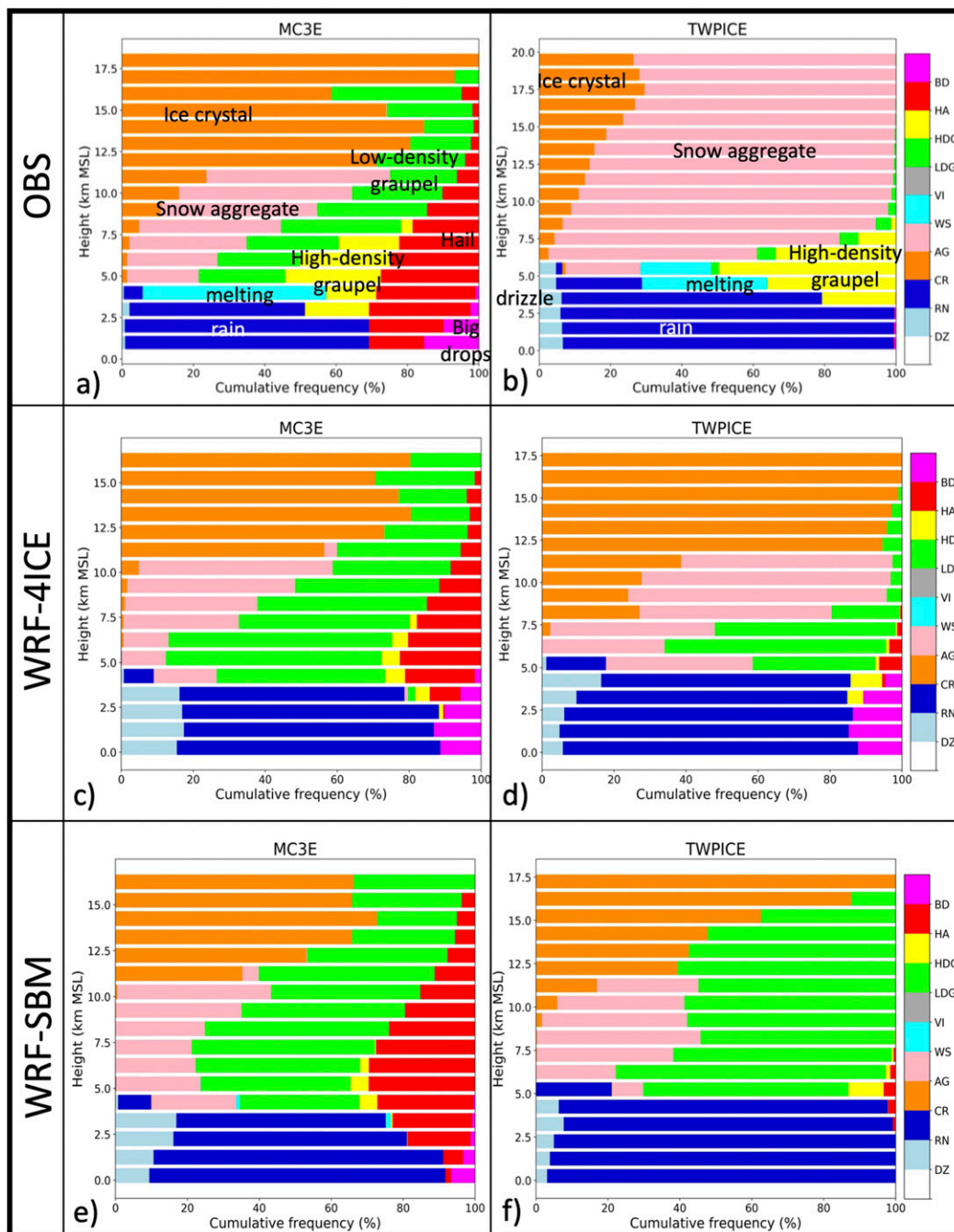


FIG. 9. (top) Stacked frequency by altitude diagrams (SFADs) of hydrometeor identification (HID) from the radar observations for the (a) MC3E and (b) TWIPICE cases. (middle) HID SFADs from the WRF-4ICE for the (c) MC3E and (d) TWIPICE cases. (bottom) HID SFADs from the WRF-SBM for the (e) MC3E and (f) TWIPICE cases.

Figures 8a and 8b show CFADs of the specific differential phase K_{dp} ($^{\circ}\text{km}^{-1}$). The specific differential phase K_{dp} is related to the mass- (or number) weighted mean oblateness, and essentially unaffected by the attenuation issue. Distributions of K_{dp}

are somewhat similar to those of Z_{dr} . However, the MC3E–TWIPICE difference plot shows K_{dp} for TWIPICE is consistently larger than MC3E, especially below 4 km (Fig. 8c), likely indicating larger water contents in the maritime case. In contrast, MC3E Z_{dr} values shift

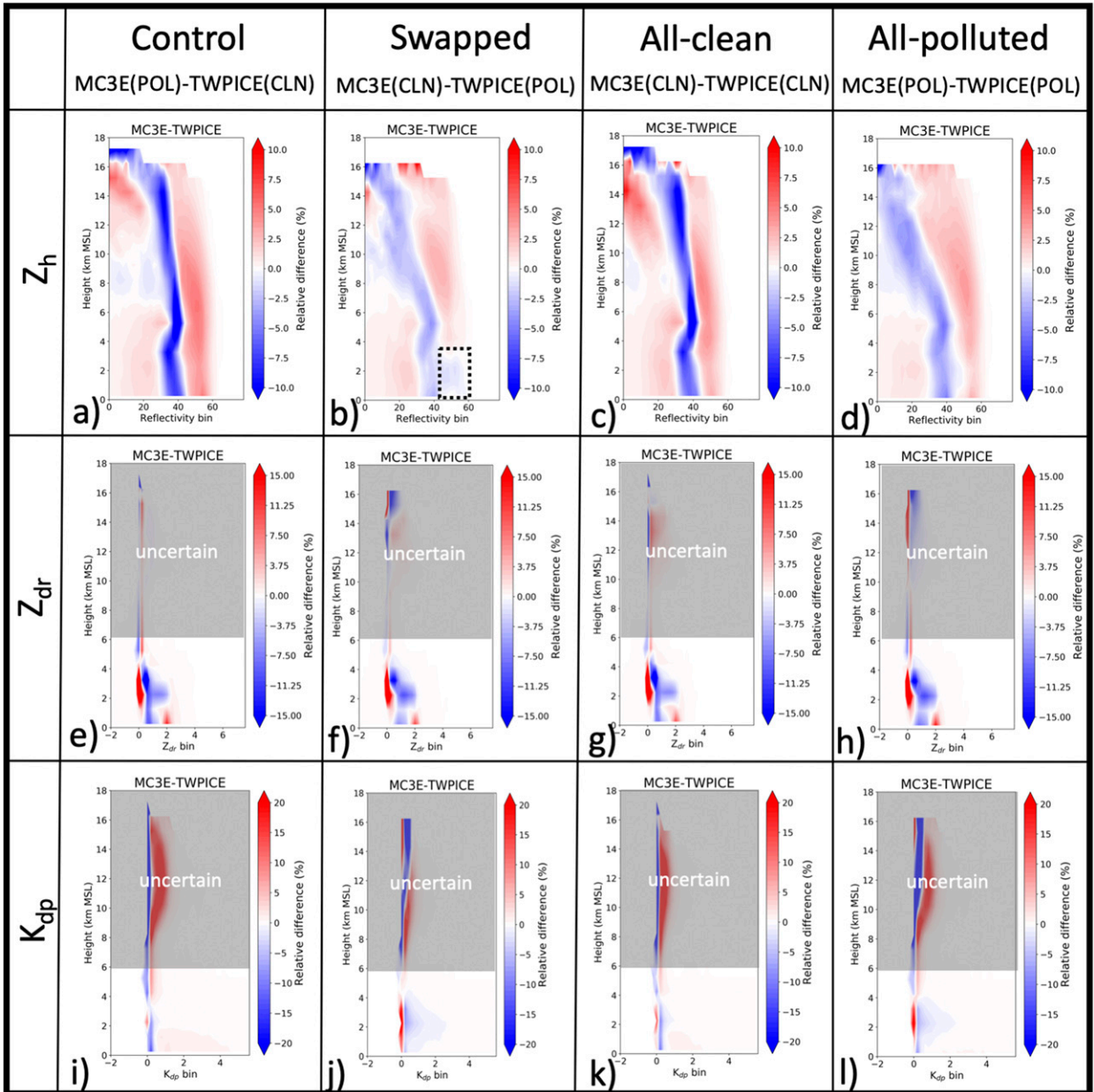


FIG. 10. MC3E-TWP contrast of POLARRIS-simulated Z_h , Z_{dr} , and K_{dp} CFADS from the WRF-SBM sensitivity simulations for the control, swapped, all-clean, and all-polluted cases.

to either smaller or larger Z_{dr} values below 2 km (Fig. 7c). This suggests the MC3E convective cores are likely characterized by fewer numbers of larger, more oblate-shaped precipitation particles, which is reflected in Z_{dr} , but not K_{dp} , which is more closely related to particle oblateness associated with the liquid water content. Detailed rain drop size distributions are discussed in section 3c. Note that these L-O contrasts in Z_h , Z_{dr} , and K_{dp} are very similar, even if the sampling periods are extended beyond the

selected cases during the MC3E and the TWPICE campaigns.

All of these polarimetric measurements can be combined to identify the bulk hydrometeor types for each grid point (Dolan and Rutledge 2009; Dolan et al. 2013). The hydrometeor identification (HID) is stratified in the vertical level to construct stacked frequency by altitude diagrams (SFADs) of HID for the MC3E and TWPICE cases (Fig. 9). The HID SFAD for the MC3E convective cores (Fig. 9a) is characterized by a much larger fraction

of rimed hydrometeors (hail, big drops, low-/high-density graupel), while snow aggregates are the dominant species in the TWPICE case (Fig. 9b) though with a large fraction of high-density graupel concentrated near the melting layer. Below the melting layer (~ 5 -km level), there are almost no big drops nor hail categories in the TWPICE case, but they account for more than 20% in the MC3E case. These HID analyses retrieved from the ground-based polarimetric radars support the previous assumptions from the satellite observations that continental deep convective cores are characterized by more rimed particles and intense surface rainfall than maritime deep convection (Williams and Stanfill 2002; Zipser et al. 2006; Stolz et al. 2015; MA16).

b. Numerical analysis

The Z_h CFADs calculated with POLARRIS-f from WRF-4ICE and WRF-SBM are compared in the second and third row of Fig. 6 between the MC3E and TWPICE cases. Again, convective elements are defined using the same method based on simulated reflectivity intensity and sharpness (Steiner et al. 1995). The 4ICE and SBM schemes both reproduce very strong radar reflectivities (up to 60 dBZ) near the surface for both the MC3E and TWPICE cases (Figs. 6d,g). Above the freezing levels (4 km in MC3E and 6 km in TWPICE), reflectivities exceed 50 dBZ for MC3E, consistent with the presence of graupel and hail aloft in the 4ICE and SBM simulations, while the majority of reflectivities are confined below 40 dBZ for TWPICE (Figs. 6e,h). As a result, MC3E–TWPICE differences highlight the stronger reflectivities in MC3E (red shading > 40 dBZ) and weaker reflectivities in TWPICE (blue shading < 30 – 40 dBZ) above the freezing layer (Figs. 6f,i) consistent with the observations (Fig. 6c). For the SBM, the TWPICE reflectivities are more narrowly concentrated than those of MC3E throughout the profile, displaying a red–blue–red shade pattern from weak to strong reflectivities, and the TWPICE near-surface reflectivities for 4ICE are slightly stronger than for MC3E due to large raindrops in the TWPICE 4ICE simulation (Fig. 6f, dotted box).

Compared to MA16, overall, the L–O contrast of the reflectivity CFADs generated by the 4ICE scheme here are in better agreement than that derived from the MMF-4ICE simulation (Fig. 7b of MA16), probably because of the model dimension (3D in the WRF versus 2D grid in the MMF) and resolution (1 km in the WRF versus 4-km grid spacing in the MMF). Similar to our previous study (Iguchi et al. 2012a,b), SBM again tends to overestimate reflectivities above the 8-km level probably due to the overproduction of rimed particles (discussed later in Fig. 9).

In Fig. 7, Z_{DR} CFADs calculated with POLARRIS-f from the WRF simulations for the MC3E and TWPICE cases are compared. Below 6 km, the 4ICE CFAD distributions are broader (Figs. 7d,e) and the SBM narrower (Figs. 7g,h), but both the 4ICE and SBM schemes generally capture the observed L–O contrast patterns (Figs. 7f,i, red–blue–red transitions from weak to strong Z_{dr}) with larger, flatter raindrops present in MC3E. However, the 4ICE TWPICE simulation results in a secondary concentration (Fig. 7f, dotted box) of high Z_{dr} (~ 4), which is larger than MC3E. This is likely due to an overestimation of raindrop sizes in the 4ICE scheme and is consistent with the overestimated low-level Z_h for TWPICE (Fig. 6f, dotted box). The 4ICE scheme is a single-moment scheme that essentially follows the prescribed size distributions as a function of drop size distribution formulae. Thus, unlike SBM, 4ICE does not explicitly account for raindrop break up process, and overestimated rain drop mass results in overestimated rain drop sizes. Also in POLARRIS, a larger axis ratio is assumed for large rain drops based on the empirical relationship of Brandes et al. (2002). This eventually characterizes the larger rain drop mass always lead to larger Z_{dr} in 4ICE.

In Fig. 8, K_{dp} CFADs calculated with POLLARRIS-f from the WRF simulations are compared for the MC3E and TWPICE cases. In contrast to Z_{dr} , K_{dp} is particle oblateness weighted toward particle total mass (or number concentration) (Bringi and Chandrasekar 2001). The simulated K_{dp} CFADs generally capture the observed patterns below 6 km (Figs. 8d,e,g,h). But, below the melting level, only the 4ICE scheme slightly agrees with the observed L–O composites (Fig. 8f), while the SBM scheme is opposite of the observed L–O contrast with larger K_{dp} values for the MC3E case (Fig. 8i) as a result of underestimating frequencies of high K_{dp} values for TWPICE (Fig. 8h). This bias suggests potential biases in rain drop size distributions in the WRF-SBM simulation (discussed in section 3c).

Figures 9c–f show iPOLARRIS-calculated HID SFADs from the WRF simulations for the MC3E and TWPICE cases. HID SFADs represent the fractional coverage of bulk hydrometeor types at each different height level and are suitable for evaluating the bulk hydrometeor structure of convective systems (Matsui et al. 2019). It should again be noted that this is not directly derived from the simulated bulk hydrometeor mass concentrations; instead, this is derived from the POLARRIS-f-calculated polarimetric radar observables using the HID retrieval in identical manner to the observations (Dolan et al. 2013).

Both the 4ICE and SBM schemes show similar and realistic distributions of bulk hydrometeor types for the

MC3E case (Figs. 9c,e). However, both simulations tend to overestimate the graupel fractions compared to the observed HID SFADs (Fig. 9a). In the TWPICE case, the 4ICE and SBM schemes both largely underestimate the fraction of snow aggregates versus the observations (Figs. 9b,d,f). Especially in the 4ICE scheme, a large amount of snow aggregates was categorized as “ice crystals” due to smaller sizes (Matsui et al. 2019). For the SBM scheme, the problem is due to a greatly overestimated fraction of rimed particles. The TWPICE 4ICE simulation overestimated the fraction of big drops near the surface as also reflected in the biases in Z_h and Z_{dr} there (Figs. 6e, 7e). The 4ICE scheme also tends to have a larger fraction of big drops in MC3E than observed. Again, this is due to the fact that the 4ICE scheme uses a fixed intercept for larger raindrops [smaller sizes are adjusted to mitigate excessive rain evaporation using a bin-based correction factor, see Lang et al. (2014) for details]. Thus, for larger rain amounts, rain drop size tends to be unrealistically large without explicitly considering the impact of raindrop break up.

c. Sensitivity of polarimetric signals to background aerosol concentrations

This section discusses the sensitivity of polarimetric radar L-O contrast to the background aerosols. As mentioned, previous observational studies discussed the impact of the thermodynamic effect, mesoscale dynamics effects, and aerosols for characterizing continental and maritime deep convection. Robinson et al. (2011) concluded that continental convective vigor can be reproduced by the thermal-patch effect without changing the background aerosols. MA16 also used bulk microphysics to generate some features of continental convective vigor without considering any aerosol impacts. Liu et al. (2019) demonstrated predicting the L-O contrast of the high-flash thunderstorm using multiple thermodynamic parameters. However, these studies did not directly investigate the role of aerosols on the manifestation of L-O contrast for deep convection, and indeed, many observational and modeling studies support convective vigor due to increased amounts of background aerosols (summarized in Tao et al. 2012; Fan et al. 2016).

Here, WRF-SBM is used to conduct aerosol sensitivity tests, because aerosol–cloud interactions are explicitly accounted for with detailed droplet nucleation and size-resolved microphysics processes (e.g., Khain et al. 2011; Iguchi et al. (2019, manuscript submitted to *J. Geophys. Res. Atmos.*), whereas single-moment 4ICE scheme does not account for aerosol–cloud interaction explicitly. In the control simulation, WRF-SBM background aerosol concentrations are from MERRA2 in the corresponding time and space of the MC3E

and TWPICE cases [i.e., the MC3E simulation with polluted continental aerosol concentrations, denoted as MC3E(POL), and the TWPICE simulation with clean maritime aerosol concentrations, denoted as TWPICE(CLN)]. Another set of simulations is performed by swapping the background aerosols [i.e., the MC3E simulation with clean maritime aerosol concentrations, denoted as MC3E(CLN), and the TWPICE simulation with polluted continental aerosols, denoted as TWPICE(POL) (Table 1)]. More detailed aerosol sensitivity experiments and results are discussed in Iguchi et al. (2019, manuscript submitted to *J. Geophys. Res. Atmos.*). All of results in this section are obtained from hourly output from the WRF-SBM simulations due to disk limitations.

Figure 10 shows four different combinations of MC3E–TWPICE differences in Z_h CFADs. The composites between MC3E(POL) and TWPICE (CLN) (Figs. 10a,e,i) represent the *control* and are identical to the previous section (but with less sampling density in time), while the difference between the MC3E(CLN) and TWPICE (POL) cases is denoted as *swapped*, since the background aerosols are swapped between the two cases (Figs. 10b,f,j). A clean-aerosol contrast [MC3E(CLN)–TWPICE (CLN)] is denoted as *all-clean* (Figs. 10c,g,k), while a polluted-aerosol contrast [MC3E(POL)–TWPICE (POL)] is denoted as *all-polluted* (Figs. 10d,h,l).

L-O Z_h CFADs for the control and all-clean cases are very similar to each other (Figs. 10a,c), suggesting the impact of aerosols on the MC3E case is very small for Z_h (hence particle size). This limited response of deep convection in the continental midlatitude environment was also suggested by previous observational studies (e.g., Khain et al. 2008) and recent modeling studies (Iguchi et al. 2019, manuscript submitted to *J. Geophys. Res. Atmos.*) due to the dominant role of background thermodynamics on droplet nucleation.

On the other hand, increasing aerosols in the TWPICE case appears to have a stronger impact, modulating the L-O contrast patterns in the TWPICE case by broadening the reflectivity distributions above 8 km and reducing the differences with MC3E in both the swapped and all-polluted cases (Figs. 10b,d). Below the 2-km level, TWPICE (POL) exceeds the frequency of stronger radar reflectivities greater than 40 dBZ in swapped case (Fig. 10b, dotted box). The swapped case overall weakens the L-O contrast in the reflectivity CFADs in comparison with the control case. In other words, this indicates that realistic initialization of background aerosols in maritime environment support creating more realistic L-O contrast patterns of reflectivity from the convective cores.

This statement can be also applied to Z_{dr} , but the K_{dp} , Z_{dr} L-O contrast patterns below 6 km are nearly the

same regardless of the background (Figs. 10e–h); however, the K_{dp} patterns change for the polluted TWPIECE case (Figs. 10i–l). The polluted case comparison (the swapped and all-polluted) actually shows more realistic L–O contrast composites (Figs. 10j,l). Indeed, the different responses in Z_{dr} and K_{dp} to the background aerosol concentrations are of interest and intriguing. Rain drop sizes and axis ratios have been studied for a long time, and the relationship used in this study (Brandes et al. 2002) has been a commonly used formula (e.g., Applied Radar Science Group 2019). If the size–oblateness relationship is physically reasonable, this implies the WRF–SBM scheme is not reproducing the correct raindrop size distributions for the MC3E and/or TWPIECE cases.

For clarity, surface rain drop size distributions (DSD) from the WRF–SBM simulations are compared with those from the surface disdrometer (Fig. 2). Specifically, the MC3E data are from two-dimensional video disdrometers (2DVDs), while the TWPIECE data are from a Joss–Waldvogel disdrometer (JWD). DSDs are constructed from the means of 1-min DSDs with a threshold of 100 drops. To gain enough sampling from the ground-based instrument, rain DSDs are sampled from 3 November 2005 to 10 February 2006 for TWPIECE and from 23 April to 25 May 2011 for MC3E. Since the sampling scales are completely different between the ground-based disdrometers and the scanning radars, a radar-based convective–stratiform separation method cannot be applied to the disdrometer data. Instead, rain DSDs are sampled for strong surface rain rates ($>15 \text{ mm h}^{-1}$) to select convective points. Corresponding rain DSDs are sampled from the entire domain of the hourly outputs in the WRF–SBM sensitivity experiments with the same rain rate threshold ($>15 \text{ mm h}^{-1}$). Figure 11 shows rain DSDs from observations and the WRF–SBM sensitivity experiments. The observations clearly show the L–O contrast in rain DSDs with MC3E having more concentrations of larger rain drops ($>4 \text{ mm}$) and very small rain drops ($<1 \text{ mm}$), while TWPIECE has a greater concentration of small sized (1–3 mm) rain drops. These rain DSDs clearly explain the observed radar contrast at the near-surface level.

The rain DSDs from the WRF–SBM control simulations, MC3E(POL) and TWPIECE(CLN), both show L–O contrast in similar way to observations, although very large rain drops ($>6 \text{ mm}$) are overestimated in both control simulations (thin red and blue solid lines in Fig. 10) most likely due to underestimation of instantaneous breakup of large raindrops (Iguchi et al. 2012b). This may lead the biases in the simulated K_{dp} distributions in the WRF–SBM simulations (Figs. 8, 10). When the background aerosols are swapped in MC3E(CLN)

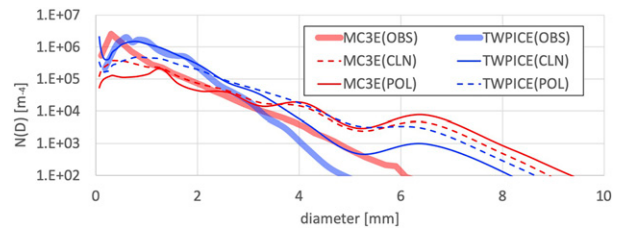


FIG. 11. Surface rain drop size distributions from the disdrometers (thick lines) and the WRF–SBM simulations (thin solid and dash lines) for the MC3E (red) and the TWPIECE (blue) cases.

and TWPIECE(POL), the surface rain DSDs become very similar between the two experiments with less L–O contrast especially for larger drop concentrations. The TWPIECE(POL) case exhibits a decrease in small and moderately sized drops and an increase in larger drops, aligning it more with the continental DSDs. Changes to the MC3E DSDs when modifying the background aerosols shows a small increase in small drop numbers and a corresponding decrease in bigger drops. However, as seen in the other findings, the continental environment is less sensitive to changes in aerosols in comparison with the oceanic environment. Although the sampling and thresholds are not identical to the disdrometer analysis and the previous radar-based statistics, the broad comparisons made here support the previous discussions on L–O contrast.

4. Summary and discussion

This study builds on the previous findings of L–O contrasts in deep convection from modeling and observational studies by employing polarimetric radar observations and the more sophisticated CRM simulations. For this, case studies of convection from continental midlatitude (MC3E) and tropical maritime (TWPIECE) conditions were selected as the examples of the representative convection cases, although we cannot generalize these cases for all midlatitude continental and tropical maritime convections. Initial observational L–O composites from the ground-based polarimetric radar instruments clearly show L–O contrast with the continental convection having larger reflectivities, similar to the climatology from the TRMM PR CFADs (MA16), assuring the representativeness of the convective core characteristics from the two selected cases.

The Z_{dr} and K_{dp} L–O composites also characterize the unique microphysics between these two different conditions, suggesting that maritime deep convection tends to have more horizontally oriented oblate ice particles above the melting layer, while continental deep convection tends to have a smaller number of large oblate

raindrops near the surface. This is confirmed by the direct DSD measurements from surface disdrometers. HID composites are used to summarize the vertical fraction of hydrometeor types within the convective cores; continental convective cores are characterized with heavy rimed particles, while the maritime deep convection is dominated by snow aggregates. L-O composites of w suggest that continental (maritime) convection tends to have stronger (weaker) up- and downdrafts. These differences were not directly revealed by previous satellite observations (Williams and Stanfill 2002; Williams et al. 2004; Zipser et al. 2006; Stolz et al. 2015; MA16).

These two cases are also simulated using WRF with both a bulk single moment (4ICE) and size-resolved bin microphysics (SBM) scheme. Both the WRF-4ICE and WRF-SBM simulations reproduce the L-O contrasts in the reflectivity and Z_{dr} CFADs similar to the observations, but K_{dp} is not well captured by WRF-SBM for the maritime case, indicating biases in the raindrop size distributions. Both microphysics schemes also reproduce realistic L-O contrasts in bulk hydrometeor types in the convective cores, although rimed frozen particles appear to be overestimated. For a better understanding of polarimetric observables above the melting layer, the use of more advanced shape-resolved ice microphysics schemes (Hashino and Tripoli 2011; Harrington et al. 2013; Chen and Tsai 2016; Jensen et al. 2018) is encouraged in the future.

Finally, the impact of aerosols on deep convective L-O contrast has been examined from sensitivity experiments using WRF-SBM. The results demonstrate for the first time that the background continental and maritime aerosols are important for reproducing the observed L-O contrast composites. For example, when background aerosol conditions are flipped between the continental and maritime conditions, raindrop sizes (as indicated by radar reflectivity) of maritime deep convective cores mimic those in the continental deep convective cores. This indicates that aerosols play potential roles with respect to surface rainfall intensity, but thermodynamics plays the dominant role in characterizing L-O contrasts of ice microphysics within the deep convective cores. Of course, our simulations and sensitivity experiments are very limited, and robustness of our study requires further observational and numerical experiments.

It is also important to note that polarimetric radar-based model evaluation reveals some fundamental problems in CRM microphysics in representing accurate microphysical DSDs and L-O contrast beyond the traditional reflectivity-based evaluation method (e.g., Lang et al. 2014). In fact, SBM tends to produce

overly narrow distributions of K_{dp} signals near the surface, which is related to the unrealistic raindrop size distributions as compared to the disdrometer measurements. This is related to the complex ice microphysics processes, which have been improved over the past decade (Matsui et al. 2009; Li et al. 2010; Lang et al. 2014). The uncertainties in ice microphysics in deep convection are related to (i) cloud and ice nucleation processes, (ii) diffusional growth and saturation adjustment, (iii) riming and ice aggregation processes, and (iv) the breakup of large particles. Some of these biases/uncertainties in the microphysics may be related to the inaccurate representation of model dynamics, which may not truly resolve convective thermal bubbles (Hernandez-Deckers and Sherwood 2016).

In summary, this study showed that

- 1) polarimetric radar signatures have unique L-O contrasts signals, which fundamentally characterize the microphysics and kinematics between midlatitude continental and tropical maritime deep convection;
- 2) WRF POLARRIS-simulated L-O contrasts show more favorable agreement in radar reflectivity, polarimetric variables of raindrops, and hydrometeor distributions, while there are yet uncertainties in describing polarimetric observables (Z_{dr} and K_{dp}) of ice particles associated with the shapes and orientations (Matsui et al. 2019); and
- 3) the sensitivity of WRF simulations with size-resolved microphysics demonstrates importance of the background aerosols in more distinctly characterizing L-O contrasts of convective cores in addition to the impact of the background thermodynamics.

This last conclusion suggests the importance of formulating NASA's future satellite mission for Aerosol-Cloud, Convection, and Precipitation (A-CCP; National Academies of Sciences Engineering and Medicine 2018).

Acknowledgments. This work is funded by the Department of Energy (DOE) Atmospheric System Research (ASR) program (DE-SC0014371). The authors thank the DOE ASR project managers: Drs. Shaima Nasiri and Ashley Williamson. Authors are also funded by the NASA Precipitation Measurement Mission (PMM, Project Manager Gail S. Jackson) and Modeling Analysis and Prediction (MAP, Project Manager, David Considine) programs. We acknowledge Julie Barnum and Alyssa Matthews for their processing of the radar data for the field campaigns. We also thank the NASA Advanced Supercomputing (NAS) Division and Center for Climate Simulation (NCCS) (Project Manager T. Lee at NASA HQ) for providing the computational resources to conduct the WRF and POLARRIS simulations. WRF-SBM

and WRF-4ICE simulations of the MC3E case are available through the NASA GSFC Cloud Library (<https://portal.nccs.nasa.gov/cloudblibrary/>) upon request. DOE ARM radar data are available from ARM DATA DISCOVERY (<http://www.archive.arm.gov/discovery/#v/results/sfcats::sfcprop>). POLARRIS also is available to public (<http://radarmet.atmos.colostate.edu/polarris/>).

REFERENCES

- Applied Radar Science Group, 2019: User manual CR-SIM software v 3.30. Radar Science Observatory, School of Marine and Atmospheric Sciences, Stony Brook University, 93 pp., <ftp.radar.bnl.gov/outgoing/moue/crsim/docs/crsim-UserGuide-v3.3.0.pdf>.
- Brandes, E. A., G. Zhang, and J. Vivekanandan, 2002: Experiments in rainfall estimation with a polarimetric radar in a subtropical environment. *J. Appl. Meteor.*, **41**, 674–685, [https://doi.org/10.1175/1520-0450\(2002\)041<0674:EIREWA>2.0.CO;2](https://doi.org/10.1175/1520-0450(2002)041<0674:EIREWA>2.0.CO;2).
- Bringi, V., and V. Chandrasekar, 2001: *Polarimetric Doppler Weather Radar: Principles and Applications*. Cambridge University Press, 636 pp.
- Chen, J., and T. Tsai, 2016: Triple-moment modal parameterization for the adaptive growth habit of pristine ice crystals. *J. Atmos. Sci.*, **73**, 2105–2122, <https://doi.org/10.1175/JAS-D-15-0220.1>.
- Chern, J.-D., W.-K. Tao, S. E. Lang, T. Matsui, J.-L. F. Li, K. I. Mohr, G. M. Skofronick-Jackson, and C. D. Peters-Lidard, 2016: Performance of the Goddard multiscale modeling framework with Goddard ice microphysical schemes. *J. Adv. Model. Earth Syst.*, **8**, 66–95, <https://doi.org/10.1002/2015MS000469>.
- Collis, S., A. Protat, P. T. May, and C. Williams, 2013: Statistics of storm updraft velocities from TWP-ICE including verification with profiling measurements. *J. Appl. Meteor. Climatol.*, **52**, 1909–1922, <https://doi.org/10.1175/JAMC-D-12-0230.1>.
- Dolan, B., and S. A. Rutledge, 2009: A theory-based hydrometeor identification algorithm for X-band polarimetric radars. *J. Atmos. Oceanic Technol.*, **26**, 2071–2088, <https://doi.org/10.1175/2009JTECHA1208.1>.
- , —, S. Lim, V. Chandrasekar, and M. Thurai, 2013: A robust C-band hydrometeor identification algorithm and application to a long-term polarimetric radar dataset. *J. Appl. Meteor. Climatol.*, **52**, 2162–2186, <https://doi.org/10.1175/JAMC-D-12-0275.1>.
- Fan, J., Y. Wang, D. Rosenfeld, and X. Liu, 2016: Review of aerosol–cloud interactions: Mechanisms, significance, and challenges. *J. Atmos. Sci.*, **73**, 4221–4252, <https://doi.org/10.1175/JAS-D-16-0037.1>.
- Fridlind, A. M., and Coauthors, 2012: A comparison of TWP-ICE observational data with cloud-resolving model results. *J. Geophys. Res.*, **117**, D05204, <https://doi.org/10.1029/2011JD016595>.
- Grabowski, W. W., 2018: Can the impact of aerosols on deep convection be isolated from meteorological effects in atmospheric observations? *J. Atmos. Sci.*, **75**, 3347–3363, <https://doi.org/10.1175/JAS-D-18-0105.1>.
- Harrington, J. Y., K. Sulia, and H. Morrison, 2013: A method for adaptive habit prediction in bulk microphysical models. Part I: Theoretical development. *J. Atmos. Sci.*, **70**, 349–364, <https://doi.org/10.1175/JAS-D-12-040.1>.
- Hashino, T., and G. J. Tripoli, 2011: The Spectral Ice Habit Prediction System (SHIPS). Part III: Description of the ice particle model and the habit-dependent aggregation model. *J. Atmos. Sci.*, **68**, 1125–1141, <https://doi.org/10.1175/2011JAS3666.1>.
- Hernandez-Deckers, D., and S. C. Sherwood, 2016: A numerical investigation of cumulus thermals. *J. Atmos. Sci.*, **73**, 4117–4136, <https://doi.org/10.1175/JAS-D-15-0385.1>.
- Houze, R. A., and A. K. Betts, 1981: Convection in GATE. *Rev. Geophys.*, **19**, 541–576, <https://doi.org/10.1029/RG019i004p00541>.
- Iguchi, T., and Coauthors, 2012a: Numerical analysis using WRF-SBM for the cloud microphysical structures in the C3VP field campaign: Impacts of supercooled droplets and resultant riming on snow microphysics. *J. Geophys. Res.*, **117**, D23206, <https://doi.org/10.1029/2012JD018101>.
- , T. Matsui, A. Tokay, P. Kollias, and W.-K. Tao, 2012b: Two distinct modes in one-day rainfall event during MC3E field campaign: Analyses of disdrometer observations and WRF-SBM simulation. *Geophys. Res. Lett.*, **39**, L24805, <https://doi.org/10.1029/2012GL053329>.
- , and Coauthors, 2014: WRF-SBM simulations of melting layer structure in mixed-phase precipitation events observed during LPVEx. *J. Appl. Meteor. Climatol.*, **53**, 2710–2731, <https://doi.org/10.1175/JAMC-D-13-0334.1>.
- Jensen, A. A., J. Y. Harrington, and H. Morrison, 2018: Microphysical characteristics of squall-line stratiform precipitation and transition zones simulated using an ice particle property-evolving model. *Mon. Wea. Rev.*, **146**, 723–743, <https://doi.org/10.1175/MWR-D-17-0215.1>.
- Jensen, M. P., and Coauthors, 2016: The Midlatitude Continental Convective Clouds Experiment (MC3E). *Bull. Amer. Meteor. Soc.*, **97**, 1667–1686, <https://doi.org/10.1175/BAMS-D-14-00228.1>.
- Khain, A. P., D. Rosenfeld, A. Pokrovsky, U. Blahak, and A. Ryzhkov, 2011: The role of CCN in precipitation and hail in a mid-latitude storm as seen in simulations using a spectral (bin) microphysics model in a 2D dynamic frame. *Atmos. Res.*, **99**, 129–146, <https://doi.org/10.1016/j.atmosres.2010.09.015>.
- , N. BenMoshe, and A. Pokrovsky, 2008: Factors determining the impact of aerosols on surface precipitation from clouds: An attempt at classification. *J. Atmos. Sci.*, **65**, 1721–1748, <https://doi.org/10.1175/2007JAS2515.1>.
- Lang, S. E., W.-K. Tao, J.-D. Chern, D. Wu, and X. Li, 2014: Benefits of a fourth ice class in the simulated radar reflectivities of convective systems using a bulk microphysics scheme. *J. Atmos. Sci.*, **71**, 3583–3612, <https://doi.org/10.1175/JAS-D-13-0330.1>.
- Li, X., W.-K. Tao, T. Matsui, C. Liu, and H. Masunaga, 2010: Improving a spectral bin microphysical scheme using long-term TRMM satellite observations. *Quart. J. Roy. Meteor. Soc.*, **136**, 382–399, <https://doi.org/10.1002/qj.569>.
- Lin, J. C., T. Matsui, R. A. Pielke Sr., and C. Kummerow, 2006: Effects of biomass burning-derived aerosols on precipitation and clouds in the Amazon basin: A satellite-based empirical study. *J. Geophys. Res.*, **111**, D19204, <https://doi.org/10.1029/2005JD006884>.
- Liu, N., C. Liu, and P. E. Tisot, 2019: A Bayesian-like approach to describe the regional variation of high-flash rate thunderstorms from thermodynamic and kinematic environment variables. *J. Geophys. Res. Atmos.*, **124**, 12 507–12 522, <https://doi.org/10.1029/2019JD031254>.
- Lucas, C., E. J. Zipser, and M. A. Lemone, 1994: Vertical velocity in oceanic convection off tropical Australia. *J. Atmos. Sci.*, **51**, 3183–3193, [https://doi.org/10.1175/1520-0469\(1994\)051<3183:VVIOCO>2.0.CO;2](https://doi.org/10.1175/1520-0469(1994)051<3183:VVIOCO>2.0.CO;2).
- Masunaga, H., and C. D. Kummerow, 2006: Observations of tropical precipitating clouds ranging from shallow to deep

- convective systems. *Geophys. Res. Lett.*, **33**, L16805, <https://doi.org/10.1029/2006GL026547>.
- Matsui, T., X. Zeng, W.-K. Tao, H. Masunaga, W. Olson, and S. Lang, 2009: Evaluation of long-term cloud-resolving model simulations using satellite radiance observations and multi-frequency satellite simulators. *J. Atmos. Oceanic Technol.*, **26**, 1261–1274, <https://doi.org/10.1175/2008JTECHA1168.1>.
- , J.-D. Chern, W.-K. Tao, S. Lang, M. Satoh, T. Hashino, and T. Kubota, 2016: On the land–ocean contrast of tropical convection and microphysics statistics derived from TRMM satellite signals and global storm-resolving models. *J. Hydrometeorol.*, **17**, 1425–1445, <https://doi.org/10.1175/JHM-D-15-0111.1>.
- , B. Dolan, S. A. Rutledge, W.-K. Tao, T. Iguchi, J. Barnum, and S. Lang, 2019: POLARRIS: POLARimetric Radar Retrieval and Instrument Simulator. *J. Geophys. Res. Atmos.*, **124**, 4634–4657, <https://doi.org/10.1029/2018JD028317>.
- May, P. T., J. H. Mather, G. Vaughan, K. N. Bower, C. Jakob, G. M. McFarquhar, and G. G. Mace, 2008: The Tropical Warm Pool International Cloud Experiment. *Bull. Amer. Meteor. Soc.*, **89**, 629–645, <https://doi.org/10.1175/BAMS-89-5-629>.
- Michalakes, J., S. Chen, J. Dudhia, L. Hart, J. Klemp, J. Middlecoff, and W. Skamarock, 2001: Development of a next generation regional weather research and forecast model. *Developments in Teracomputing: Proceedings of the Ninth ECMWF Workshop on the Use of High Performance Computing in Meteorology*, W. Zwiefelhofer and N. Kreitz, Eds., World Scientific, 269–276.
- Morton, B. R., G. I. Taylor, and J. S. Turner, 1956: Turbulent gravitational convection from maintained and instantaneous sources. *Proc. Roy. Soc. London*, **234A**, 1–23, <https://doi.org/10.1098/RSPA.1956.0011>.
- National Academies of Sciences, Engineering, and Medicine, 2018: *Thriving on Our Changing Planet: A Decadal Strategy for Earth Observation from Space*. National Academies Press, 716 pp.
- Randles, C. A. A. M., and Coauthors, 2016: The MERRA-2 aerosol assimilation. NASA Tech. Memo. NASA/TM-2016-104606/Vol. 45, 140 pp., <https://gmao.gsfc.nasa.gov/pubs/docs/Randles887.pdf>.
- Robinson, F., S. Sherwood, D. Gerstle, C. Liu, and D. Kirshbaum, 2011: Exploring the land–ocean contrast in convective vigor using islands. *J. Atmos. Sci.*, **68**, 602–618, <https://doi.org/10.1175/2010JAS3558.1>.
- Ryzhkov, A., M. Pinsky, A. Pokrovsky, and A. Khain, 2011: Polarimetric radar observation operator for a cloud model with spectral microphysics. *J. Appl. Meteor. Climatol.*, **50**, 873–894, <https://doi.org/10.1175/2010JAMC2363.1>.
- Seinfeld, J. H., and S. N. Pandis, 2006: *Atmospheric Chemistry and Physics: From Air Pollution to Climate Change*. 2nd ed. John Wiley & Sons, 1232 pp.
- Skamarock, W. C., and Coauthors, 2008: A description of the Advanced Research WRF version 3. NCAR Tech. Note NCAR/TN-4751STR, 113 pp., <https://doi.org/10.5065/D68S4MVH>.
- Steiner, M., R. A. Houze Jr., and S. E. Yuter, 1995: Climatological characterization of three-dimensional storm structure from operational radar and rain gauge data. *J. Appl. Meteor.*, **34**, 1978–2007, [https://doi.org/10.1175/1520-0450\(1995\)034<1978:CCOTDS>2.0.CO;2](https://doi.org/10.1175/1520-0450(1995)034<1978:CCOTDS>2.0.CO;2).
- Stolz, D. C., S. A. Rutledge, and J. R. Pierce, 2015: Simultaneous influences of thermodynamics and aerosols on deep convection and lightning in the tropics. *J. Geophys. Res. Atmos.*, **120**, 6207–6231, <https://doi.org/10.1002/2014JD023033>.
- Tao, W.-K., and J.-D. Chern, 2017: The impact of simulated mesoscale convective systems on global precipitation: A multi-scale modeling study. *J. Adv. Model. Earth Syst.*, **9**, 790–809, <https://doi.org/10.1002/2016MS000836>.
- , J.-P. Chen, Z. Li, C. Wang, and C. Zhang, 2012: Impact of aerosols on convective clouds and precipitation. *Rev. Geophys.*, **50**, RG2001, <https://doi.org/10.1029/2011RG000369>.
- , D. Wu, S. Lang, J.-D. Chern, C. Peters-Lidard, A. Fridlind, and T. Matsui, 2016: High-resolution NU-WRF simulations of a deep convective-precipitation system during MC3E: Further improvements and comparisons between Goddard microphysics schemes and observations. *J. Geophys. Res. Atmos.*, **121**, 1278–1305, <https://doi.org/10.1002/2015JD023986>.
- Varble, A., and Coauthors, 2014: Evaluation of cloud-resolving and limited area model intercomparison simulations using TWP-ICE observations: 1. Deep convective updraft properties. *J. Geophys. Res. Atmos.*, **119**, 13 891–13 918, <https://doi.org/10.1002/2013JD021371>.
- Vivekanandan, J., W. M. Adams, and V. N. Bringi, 1991: Rigorous approach to polarimetric radar modeling of hydrometeor orientation distributions. *J. Appl. Meteor.*, **30**, 1053–1063, [https://doi.org/10.1175/1520-0450\(1991\)030<1053:RATPRM>2.0.CO;2](https://doi.org/10.1175/1520-0450(1991)030<1053:RATPRM>2.0.CO;2).
- Wang, D., S. E. Giangrande, K. Schiro, M. P. Jensen, and R. A. Houze, 2019: The characteristics of tropical and midlatitude mesoscale convective systems as revealed by radar wind profilers. *J. Geophys. Res. Atmos.*, **124**, 4601–4619, <https://doi.org/10.1029/2018JD030087>.
- Williams, E., and S. Stanfill, 2002: The physical origin of the land–ocean contrast in lightning activity. *C. R. Phys.*, **3**, 1277–1292, [https://doi.org/10.1016/S1631-0705\(02\)01407-X](https://doi.org/10.1016/S1631-0705(02)01407-X).
- , T. Chan, and D. Boccippio, 2004: Islands as miniature continents: Another look at the land–ocean lightning contrast. *J. Geophys. Res.*, **109**, D16206, <https://doi.org/10.1029/2003JD003833>.
- , V. Mushtak, D. Rosenfeld, S. Goodman, and D. Boccippio, 2005: Thermodynamic conditions favorable to superlative thunderstorm updraft, mixed phase microphysics and lightning flash rate. *Atmos. Res.*, **76**, 288–306, <https://doi.org/10.1016/j.atmosres.2004.11.009>.
- Winker, D. M., J. L. Tackett, B. J. Getzewich, Z. Liu, M. A. Vaughan, and R. R. Rogers, 2013: The global 3-D distribution of tropospheric aerosols as characterized by CALIOP. *Atmos. Chem. Phys.*, **13**, 3345–3361, <https://doi.org/10.5194/acp-13-3345-2013>.
- Yuter, S. E., and R. A. Houze Jr., 1995: Three-dimensional kinematic and microphysical evolution of Florida cumulonimbus. Part II: Frequency distributions of vertical velocity, reflectivity and differential reflectivity. *Mon. Wea. Rev.*, **123**, 1941–1963, [https://doi.org/10.1175/1520-0493\(1995\)123<1941:TDKAME>2.0.CO;2](https://doi.org/10.1175/1520-0493(1995)123<1941:TDKAME>2.0.CO;2).
- Zhu, P., and Coauthors, 2012: A limited area model (LAM) intercomparison study of a TWP-ICE active monsoon mesoscale convective event. *J. Geophys. Res.*, **117**, D11208, <https://doi.org/10.1029/2011JD016447>.
- Zipsper, E. J., C. Liu, D. J. Cecil, S. W. Nesbitt, and D. P. Yorty, 2006: Where are the most intense thunderstorms on Earth? *Bull. Amer. Meteor. Soc.*, **87**, 1057–1072, <https://doi.org/10.1175/BAMS-87-8-1057>.